Article

Study of MoS₂ Deposited by ALD on c-Si, Towards the Development of MoS₂/c-Si Heterojunction Photovoltaics

Bienlo Flora Zerbo [1,*], Mircea Modreanu [2], Ian Povey [2], Jun Lin [2], Antoine Létoublon [1], Alain Rolland [1], Laurent Pédesseau [1], Jacky Even [1], Bruno Lépine [3], Pascal Turban [3], Philippe Schieffer [3], Alain Moréac [3] and Olivier Durand [1]

1   Univ Rennes, INSA Rennes, CNRS, Institut FOTON—UMR 6082, F-35000 Rennes, France
2   Tyndall National Institute, University College Cork, Lee Maltings, Dyke Parade, T12 R5CP Cork, Ireland
3   Univ Rennes, CNRS, IPR (Institut de Physique de Rennes)—UMR 6251, F-35042 Rennes, France
*   Correspondence: bienlo.zerbo@insa-rennes.fr

Abstract: Silicon-based heterojunction (SHJ) solar cells demonstrate high efficiencies over their homojunction counterparts, revealing the potential of such technologies. We present here the first steps towards the development of molybdenum disulfide (MoS₂)/c-silicon heterojunction solar cells, consisting of a preliminary study of the MoS₂ material and numerical device simulations of MoS₂/Si heterojunction solar cells, using SILVACO ATLAS. Through the optical and structural characterization of MoS₂/SiO₂/Si samples, we found a significant sensitivity of the MoS₂ to ambient oxidation. Optical ellipsometry showed a bandgap of 1.87 eV for a 7 monolayer thick MoS₂ sample, suitable for the targeted application. Finally, we briefly introduce a device simulation and show that the MoS₂/Si heterojunction could lead to a gain in quantum efficiency, especially in the region with short wavelengths, compared with a standard a-Si/c-Si solar cell.

Keywords: 2D molybdenum disulfide; silicon heterojunctions; solar cells

Publisher's Note: MDPI stays neutral with regard to jurisdictional claims in published maps and institutional affiliations.

1. Introduction

Among single-junction solar cells, gallium arsenide (GaAs) solar cells present the highest efficiencies, reaching up to 29.1% [1]. However, due to their high cost, their use is restricted to space applications. Thus, silicon technology is the most widespread, since it benefits from relatively low costs and high efficiencies. Particularly, the HIT (heterojunction with intrinsic thin layer) is the silicon technology exhibiting the highest efficiencies of about 26.7%, without concentration [1].

The principle of a heterojunction solar cells lies in a low surface recombination velocity through the separation of the crystalline (c-Si) absorber (<100 μm) from the highly recombination active metal contacts by a passivating and wide-bandgap emitter "buffer" layer. That buffer layer should be as "transparent" as possible to the majority carriers' flow while reflecting that of the minority carriers and, therefore, should act as a selective contact for carrier extraction [2,3]. It is usually made of an hydrogenated amorphous a-Si:H layer, which displays a 1.7 eV quasi-bandgap, as compared to the smaller 1.1 eV bandgap of the c-Si, which leads to appropriate band offsets in both the conduction and valence bands, therefore giving the required barrier for minority charge carriers [4,5]. However, a-Si:H is a low conductivity material and displays a high recombination rate of electron–holes pairs. Moreover, the absorption coefficient of a-Si:H is large and leads to high optical losses, limiting the conversion of light at short wavelengths. Therefore, to overcome these limitations, a wider bandgap semiconductor could be a promising material to replace the a-Si:H.

Molybdenum disulfide (MoS₂) is a material that could meet such requirements for heterojunction solar cells with silicon, it can display a wider bandgap (up to 2.34 eV) than a-Si:H and a suitable electronic band line-up with the p-doped Si absorber [6]. It is a layered transition metal dichalcogenide (TMD), which is a material with an MX₂ structure, where

M is a transition metal and X is a chalcogen. Molybdenum disulfide is one of the most used TMDs, probably due to the natural abundance of Mo in the Earth's crust [7]. The bulk form of layered TMDs is made of a stack of 2D single(mono)-layers (ML), held together by weak Van der Waals bonds. For MoS_2, the monolayer is a stack of the S-Mo-S form, with a plane of Mo sandwiched between two planes of sulfur. Due to this structure, which consists of stacked monolayers, layered TMDs can be easily exfoliated to obtain 2D materials, and this gives rise to exceptional properties. For instance, due to the quantum confinement effect, the bandgap nature changes and goes from an indirect type for bulk MoS_2 to a direct bandgap for monolayer MoS_2 [8]. The bandgap value also increases with decreasing thickness, and while bulk MoS_2 has an indirect bandgap of 1.29 eV, the monolayer MoS_2 has a direct bandgap of 1.89eV [8–11]. MoS_2 has three known polytypes, i.e., $1T-MoS_2$, $2H-MoS_2$, and $3R-MoS_2$. $2H-MoS_2$, the most common and stable form of MoS_2, has a hexagonal structure and has been found to be naturally a n-type semiconductor [12,13].

In 2013, Tsai and al. [6] demonstrated a power conversion efficiency (PCE) of 5.23% with a $n-MoS_2$ monolayer/p-Si heterojunction solar cell, which is to date, the best PCE for solar cells using monolayer TMD. Later, in 2019, Xu et al. [14] reduced the concentration of interface defects, observing a passivating effect of monolayer MoS_2 in a ITO/p-Si/Ag solar cell structure. The power conversion efficiency (PCE) was increased from 1.1% to 4.6% with the $ITO/n-MoS_2/p-Si/Ag$ structure. Recently, Huang et al. [15] demonstrated 9.81% efficiency using thiourea doped few-layer MoS_2 /Si heterojunction solar cells.

Regarding those interesting results, we present the optical and structural characterization of thin MoS_2 layers deposited on silicon dioxide/silicon substrates as a preliminary study to developing MoS_2 /Si heterojunction solar cells. We also simulate an MoS_2/Si heterojunction solar cell device, using SILVACO ATLAS, showing the potentialities of such devices.

2. Materials and Methods

Chemical vapor deposition (CVD) of MoS_2 was performed employing $Mo(CO)_6$ (99.99%) (Versum Materials) and 1% H_2S (99.999%) in Ar (Air Products) utilizing a commercial 300 mm atomic layer deposition reactor modified with a showerhead inlet system. The reactor temperature was set at 550 °C, and the chamber pressure was maintained at ~2.2 Torr by an N_2 carrier flow of 150 standard cubic centimeters per minute (sccm). Precursor flux of the Mo source was determined by the source temperature (28 °C), and the H_2S flow was set at 10 sccm of the 1% gas mix. Growth was achieved on a selection of substrates including SiO_2 (80 nm) on HR Si and c-plane sapphire. Reproducibility and uniformity of the CVD process was found to be excellent, with a growth rate of approximately 4 nm/hour (~6 monolayer per hour). Nominal thicknesses of MoS_2 were achieved by assuming that the estimated growth rate was linear and by adjusting the growth time. Two-dimensional MoS_2 film samples with nominal thicknesses of 4, 5, and 7 monolayers (ML) were subsequently deposited on 80 nm SiO_2/Si substrates and 7 ML MoS_2 was deposited on a sapphire (Al_2O_3) transparent substrate.

Optical ellipsometry (O.E) measurements were performed on the 2D MoS_2 samples deposited on SiO_2/Si substrates at 70-degree angles of incidence using a Woollam M2000 Ellipsometer. The optical model used for spectroscopic ellipsometry analysis was $MoS_2/SiO_2/Si$ using the CompleatEase software developed by Woollam.

UV-VIS-NIR normal incidence transmittance measurements were performed on the 7 ML MoS_2 deposited on sapphire using a Perkin Elmer Lambda 950 double-beam spectrophotometer.

Raman spectra were recorded using a Renishaw Invia Reflex micro-Raman spectrometer at room temperature. The Raman mapping was collected on several sites (50 nm × 50 nm, 1 nm step). The samples were excited using a CW Modu-Laser Stellar-REN laser emitting at 514.5 nm with a power of less than 0.4 mW. The reflecting microscope objective was 50× with NA = 0.75, and the excitation spot had a diameter of 1 µm. The back-scattered light was dispersed by a monochromator with a spectral resolution of 1.4 cm^{-1}, with the light being

detected by a charge-coupled device. The typical accumulation time was 20 s. Raman shifts were calibrated using the optical phonon frequency (520.5 cm^{-1}) of the silicon monocrystal. Surface roughness was also explored through Atomic Force Microscopy (AFM), using a Bruker Innova microscope in contact mode.

Chemical composition was confirmed through X-ray photoelectron spectroscopy (XPS) performed in a vacuum chamber with a non-monochromatized Mg $K\alpha_{1,2} = 1253.6$ eV ray.

X-ray diffraction (XRD) measurements were performed using a 5-cercles Smartlab Rigaku diffractometer with Cu $K\alpha_{1,2}$ radiation ($\lambda = 0.154184$ nm) and equipped with a HyPix-3000 detector.

Simulations were performed with the SILVACO ATLAS module, software from the TCAD (Technology Computed Aided Device) family, to solve the main semiconductor equations. Here, the Poisson's equation, continuity, and drift-diffusion models are used. Simulations of an-MoS_2/Si heterojunction solar cell device have also been performed to estimate the external quantum efficiency.

3. Results and Discussion

Raman spectroscopy results are shown in Figure 1. For all samples, in the A_{1g} and E_{2g} vibration modes, the distance between two modes have been found to be 24.3 cm^{-1}, 24.78 cm^{-1} and 24.8 cm^{-1}, respectively, for 4, 5, and 7 ML. Similarly, many studies have shown that the distance between the E_{2g} and A_{1g} Raman modes is reduced when the thickness of MoS_2 is reduced [16].
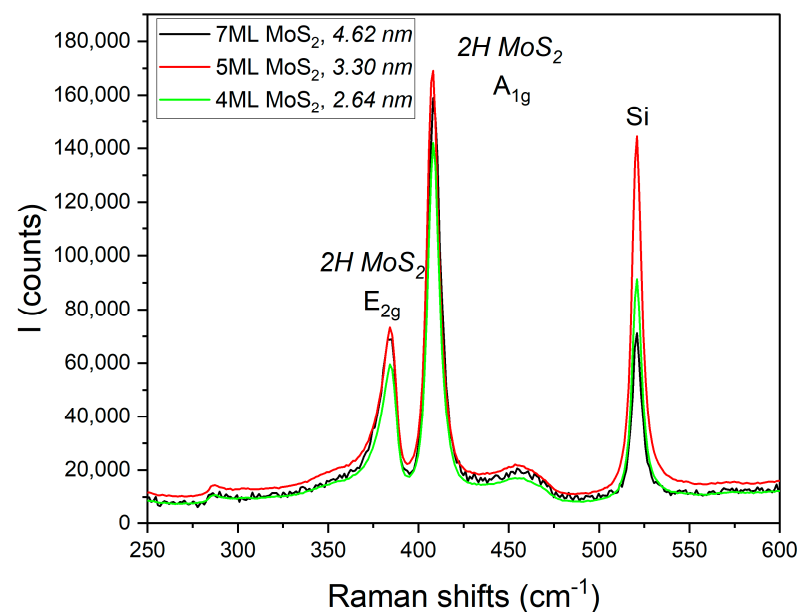

Figure 1. Raman spectra of the three samples with 4, 5, and 7 ML MoS_2.

Performing atomic force microscopy (Figures 2–4), we observe roughness in the region of 2 nm for all of the samples, which is significant relative to the thicknesses of the MoS_2 layers, which measure only a few nanometers. The AFM images also show outgrowths (yellow dots on the images), with some of them reaching about 10 nm. These outgrowths are representative of SO_2 outgassing that occur typically at MoS_2 defects and grain boundaries after prolonged exposure to air via the action of humidity to form MoS_2 MoO_{3-x}, as observed in the XPS results detailed in the next section.
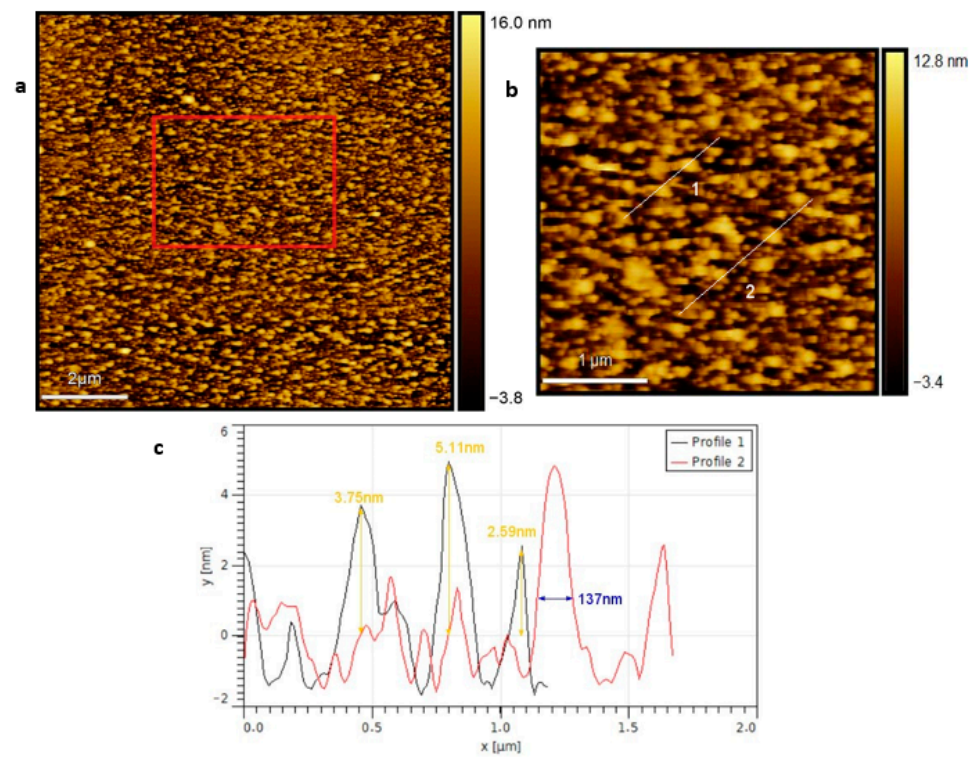
Figure 2. AFM images of 4 ML MoS₂: (**a**) 10 × 10 μm scan. (**b**) Magnified region from red box in (**a**). (**c**) Height profiles of magnified regions along lines 1 and 2 from (**b**).

Figure 3. AFM images of 5 ML MoS₂: (**a**) 10 × 10 μm scan. (**b**) Magnified region from red box in (**a**). (**c**) Height profiles of magnified regions along lines 1 and 2 from (**b**).

Figure 4. AFM images on 7 ML MoS_2: (**a**) 10×10 μm scan. (**b**) Magnified region from red box in (**a**). (**c**) Height profiles of magnified regions along lines 1 and 2 from (**b**).
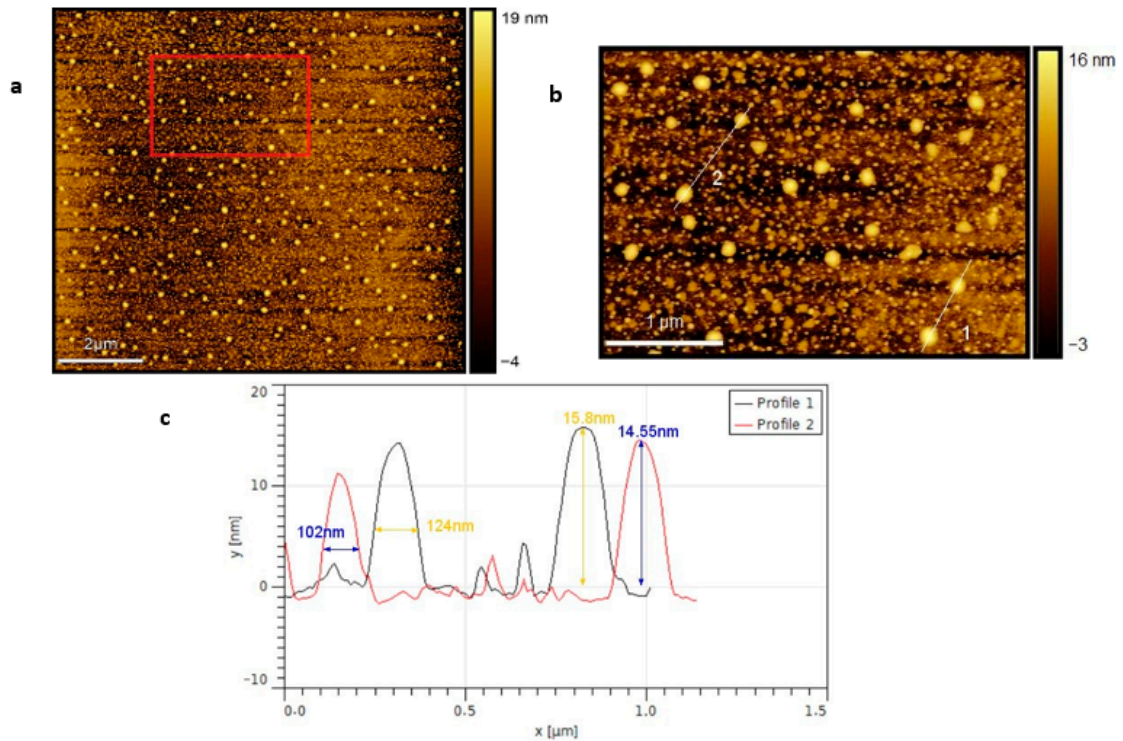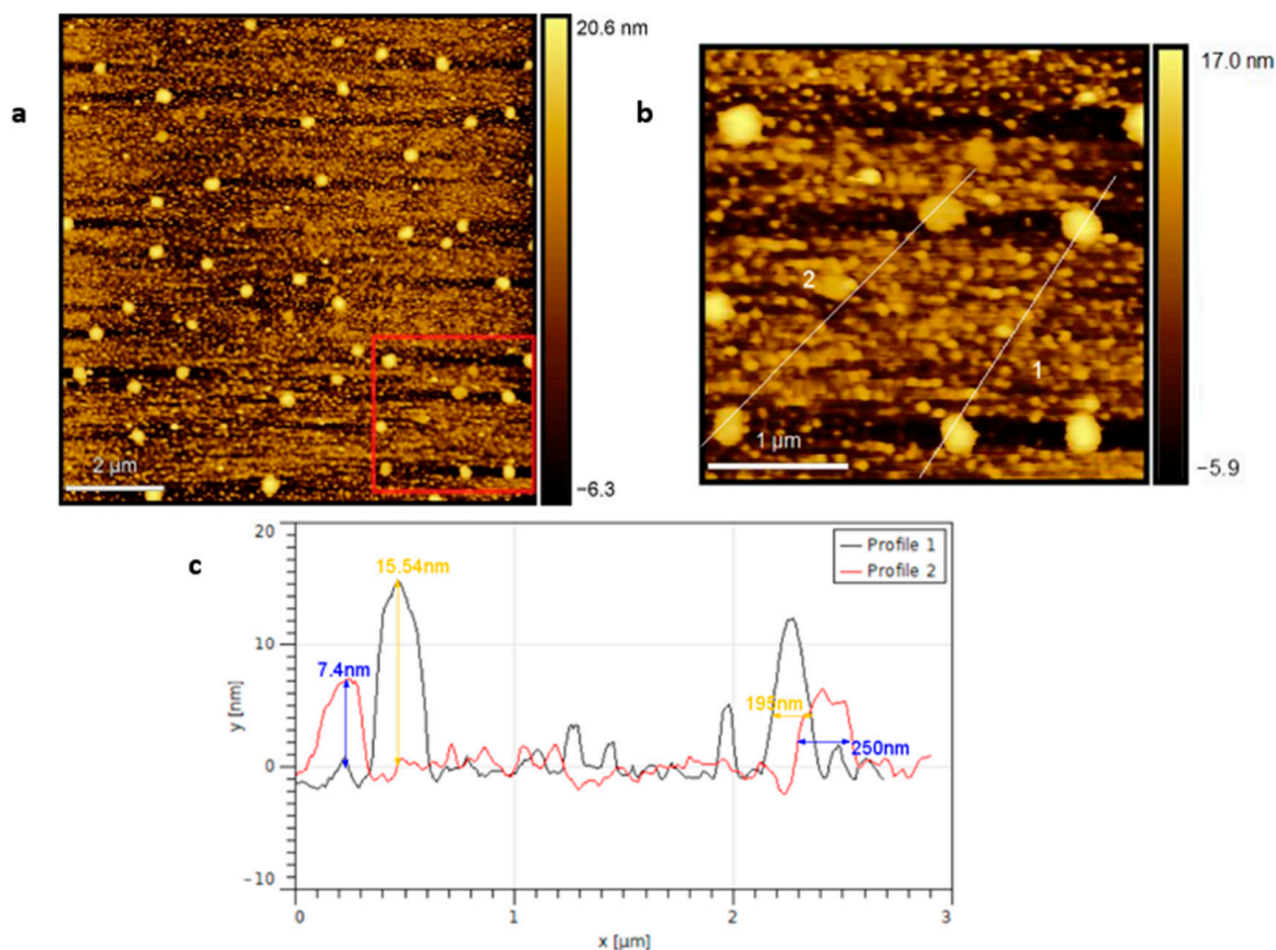
We observe the core level of molybdenum 3d, through XPS measurements that reveal the presence of different oxidation states of molybdenum in the films (Figure 5). The peak at binding energy Eb = 232.2 eV is assigned to the Mo $3d_{3/2}$ core levels. The second peak at Eb = 229.25 corresponds to the Mo $3d_{5/2}$ core levels. The two peaks are consistent with the Mo^{4+} oxidation state of 2H-MoS_2, which corresponds to stoichiometric MoS_2. The Mo^{6+} (usually attributed to MoO_3)/Mo^{5+}) oxidation states at E_b = 235.5 eV and E_b = 232.15 eV appear near the Mo^{4+} oxidation states. That would suppose that not only pure MoS_2 but also its oxidation products are present in the films. A similar phenomenon has already been described and explained in the literature [17–19]. The higher oxidation states being a consequence of exposure of MoS_2 to ambient air, such as oxidation, occurs preferentially at grain boundaries and in the defects of MoS_2, before extending throughout the film. Afanasev et al. [18] showed that MoS_2 is affected by ambient air, only after 10 min of exposure, after synthesis. The misfit between MoO_3 and MoS_2 lattices can subsequently lead to the formation of cracks [19] and outgrowths, which correspond to the AFM observations in this work. The ratio between Mo^{6+} oxidation states and the total signal of Mo 3d core levels is estimated to be about 8.1%, 12.8%, and 7.2%, respectively for 4, 5, and 7 ML MoS_2 films.
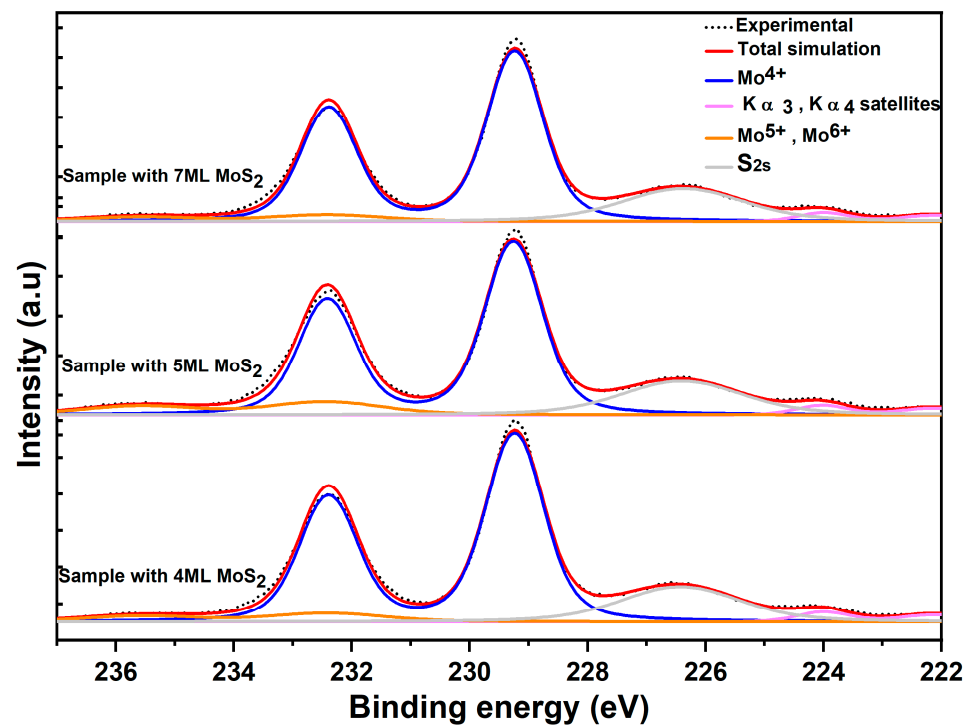
Figure 5. X-ray photoelectron spectroscopy (XPS) performed on samples with 4 ML, 5 ML and 7 ML MoS_2. The MoS_2 3d core levels are shown.

The results of the XRD (Figure 6) $\theta/2\theta$ longitudinal scans reveal a very strong texture of the MoS_2, with a preferentially orientation along the (002) planes of hexagonal MoS_2 (2H-MoS_2). That denotes a well-stacked layered structure [20]. The full width at half maximum (FWHM) values are, respectively, 4.7°, 5.1°, and 2.4° at the 2θ scale for 4, 5, and 7 ML. The (002) reflections occur at 2θ and are equal to 13.096°, 13.002°, and 13.812°, respectively, for 4, 5, and 7 ML. Pristine 2H-MoS_2 is expected to give (002) reflections at $2\theta = 14.4°$ (interlayer spacing $d_{hkl} = 0.614$ nm) [21], showing larger interlayer spacing in our case (Table 1). Moreover, using the diffraction peak FWHM β and the 2θ positions, the crystallite sizes, D, are inferred through Scherrer's equation (Equation (1)) as follows:

$$D = \frac{K\lambda}{\beta \cos \theta} \tag{1}$$

where K = 0.9 is the crystallite shape factor and $\lambda = 0.154184$ nm. The crystallite sizes are about a few nanometers, which is consistent with the thickness of the films.

Table 1. X-ray diffraction results on MoS_2 layers.

Film	2θ (°)	Inter-Reticular Spacing d (nm)	Crystallite Size (nm)
4 ML	13.096	0.676	1.7
5 ML	13.002	0.68	1.7
7 ML	13.812	0.641	3.34

However, the crystallites sizes are smaller than the film thicknesses for all samples, indicating that the deposited MoS_2 contain some structural defects that limit the size of the coherent domain of diffraction along the growth axis.

Since the optical properties of the MoS_2 layer are critical for the performance of the solar cell, we have measured the optical transmission of 7 ML MoS_2 (Figure 7) deposited on blank sapphire (Al_2O_3). From the transmission curve, we identify two absorption edges.

The first one is located at 611 nm, corresponding to an energy of 2.03 eV (B exciton), and the second absorption edge is located at 1.87 eV (A exciton).
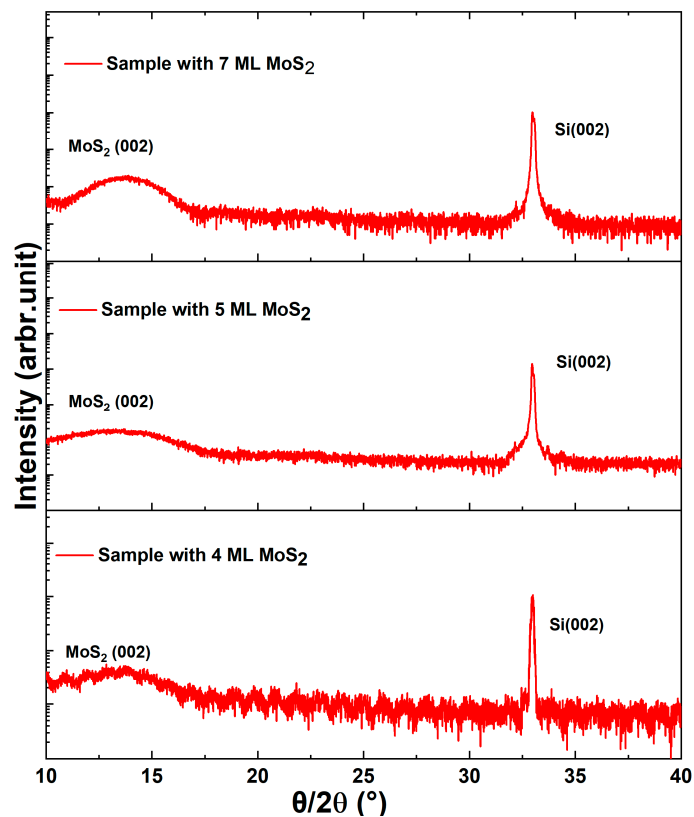

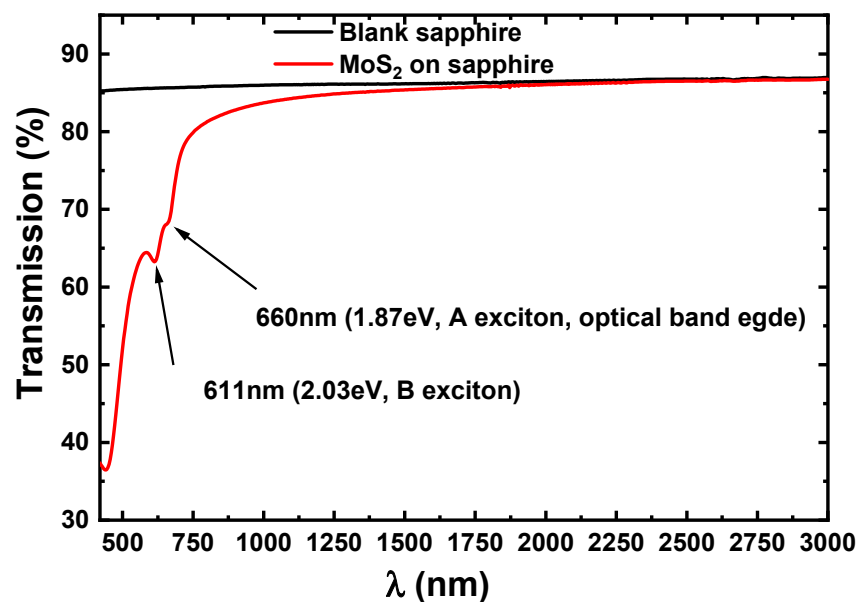**Figure 6.** X-ray diffraction on $MoS_2/SiO_2/Si$ samples.

Figure 7. Transmission of 7 ML MoS_2 deposited on sapphire.

These two excitons have already been reported in the literature for very thin to monolayer MoS_2 [8,10,22,23]. The A exciton corresponds to the optical bandgap of MoS_2. In addition to confirming the high bandgap character of MoS_2, the transmission curve

shows that MoS$_2$ would transmit most of the incoming light to the silicon substrate, even for a 7 ML-thick MoS$_2$.

The optical constants deduced from O.E. are implemented in device simulation. Most details about the implemented parameters are given in Table 2.

The simulated device architectures are kept basic since the aim of the present study is to show a proof-of-concept. For both n-MoS$_2$/p-Si and n-Si/p-Si solar cells, we assume perfect ohmic contacts. We also assume a standard AM1.5G incident light beam. Neither Intraband tunnelling nor trap-assisted tunnelling transport was taken into account. An interface recombination velocity S$_q$ = 1.10^3 cm/s is also introduced between the MoS$_2$ emitter and the Si absorber [24], and other parameters used for the calculation are given in Table 2.

We present the simulated device in Figure 8 and band alignments between n-MoS$_2$ and p-Si in Figure 9. The band alignments are shown under dark (no illumination in simulated conditions) and under light (AM 1.5 illumination). E$_c$ is the energy level of the conduction band and E$_v$ the energy level of the valence band. The Fermi level is referred to as E$_F$, in dark condition. Under illumination, the Fermi energy level splits with one for holes and one for electrons, referred to as hole quasi-fermi level (Hole QFL) and electron quasi-fermi level (Electron QFL), respectively. As one can see, the simulation shows that a type 2 heterojunction is obtained, which is favorable to carrier separation. Tsai et al. [6] have experimentally demonstrated such an heterojunction type between monolayer MoS$_2$ and Si.
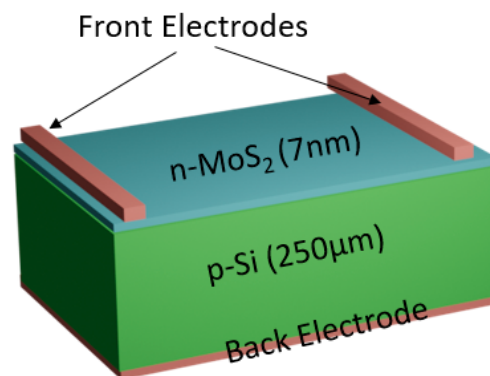

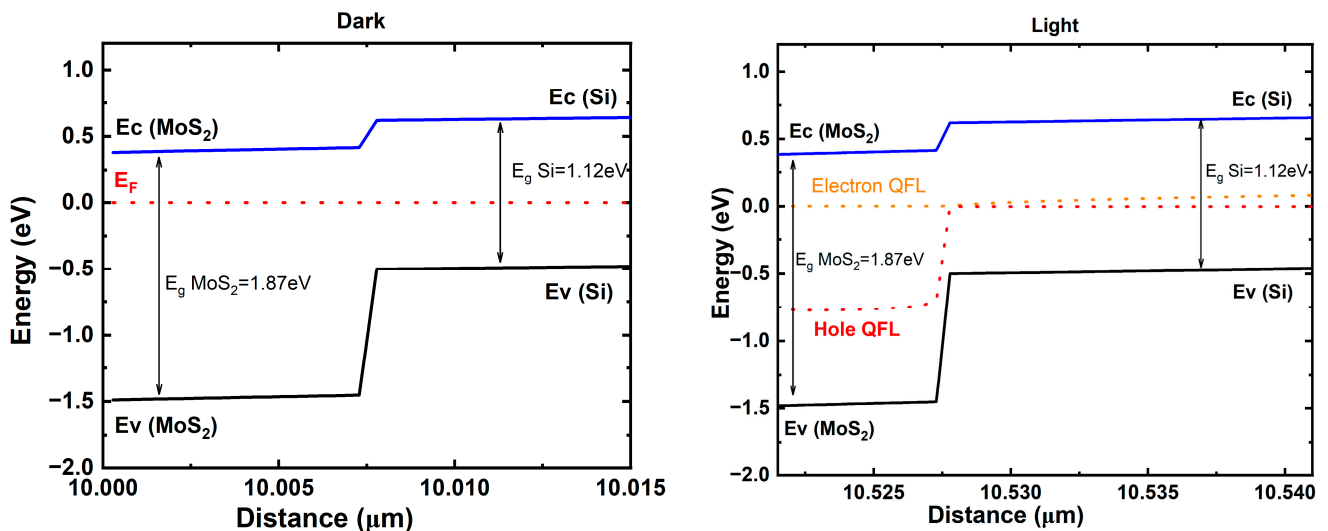**Figure 8.** Simulated n-MoS$_2$/Si heterojunction solar cell.

Figure 9. Simulated band diagram of MoS$_2$/Si heterojunction solar cell in the vicinity of the MoS$_2$/Si interface (dark and AM 1.5 light illumination, 0 Volt bias).

Figure 10 shows the results of the simulated external quantum efficiency (EQE) of MoS_2/Si solar cell. The EQE gives the number of carriers that is effectively collected over the number of incident photons, assuming that each photon produces one carrier. In Silvaco software, we calculate EQE as follows:

$$EQE = \frac{I_{electrode}}{I_s} \tag{2}$$

where $I_{electrode}$ is the current collected at the electrode and I_s is the source photocurrent given as follows:
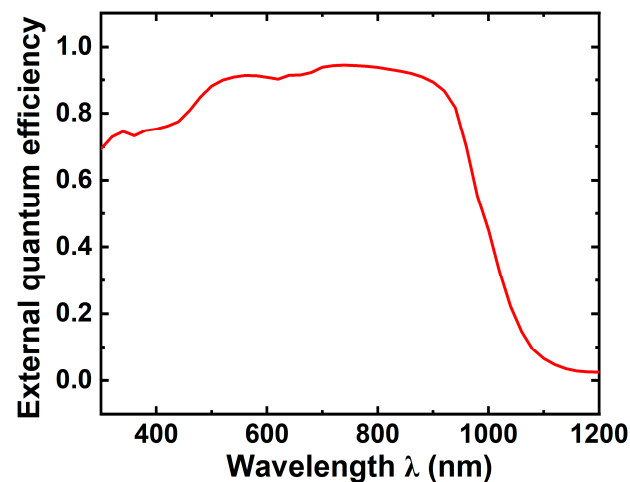
$$I_s = q\frac{B\lambda}{hc}W \tag{3}$$

Figure 10. Simulated external quantum efficiency of MoS_2/Si heterojunction solar cell.

With B as the incident beam intensity, λ as the wavelength, h as the Planck constant, c as the speed of light in a vacuum, and W as the beam width that could be defined as the rate of incident photons on the device in terms of current density.

In the short-wavelength region, the MoS_2/Si heterojunction appears to lead to a gain in EQE, as compared with standard devices [4,25]. We attribute that gain to the high bandgap of MoS_2, which limits parasitic absorption.

Table 2. Simulation parameters of n-MoS_2/p-Si heterojunction solar cell.

Material	p-Si	n-MoS_2
Thickness (μm)	250	7×10^{-3}
Bandgap (eV)	1.12	1.87
Electron affinity (eV)	4.05	4.25 [26,27]
Doping level (cm^{-3})	1×10^{16}	1×10^{14}
Permittivity	11.9	7 [28]
Electron Mobility ($cm^2 \cdot V^{-1} \cdot S^{-1}$)	1350	44 [29]
Hole mobility	500	86 [29]
Effective conduction band density Nc (cm^{-3})	2.8×10^{19}	2.5×10^{20}

4. Conclusions

We have investigated the optical and structural properties of thin 2H-MoS_2 and performed a device simulation for a MoS_2/Si heterojunction solar cell. Through AFM measurements, we have shown the rough morphology of the sample surface, with the presence of grains, holes, and outgrowths, which we attribute to the consequences of

ambient oxidation, as confirmed by XPS. Raman spectroscopy measurements have shown the multi-layer character of the samples. Regarding XRD measurements, the interlayer spacing is higher than what is reported in the literature, which we could also attribute to the presence of oxides resulting from ambient oxidation. Optical ellipsometry (O.E) measurements show the high bandgap character of MoS_2, which would make it suitable for heterojunction solar cells with silicon. O.E also provided optical constants that were integrated into a simple device simulation that indicated that using n-MoS_2 would permit a potential gain in quantum efficiency, due to the high bandgap of ~1.87 eV MoS_2, for a MoS_2/Si heterojunction solar cell, with the formation of type 2 heterojunction. Due to the observations in this work, we plan to use MoS_2 samples with an ITO capping layer to prevent the oxidation and degradation of MoS_2 and, consequently, to improve the viability of MoS_2/Si heterojunction solar cells.

Institutional Review Board Statement: Not applicable.

Informed Consent Statement: Not applicable.

Data Availability Statement: The data that support the findings of this study are available upon reasonable request from the authors.

Conflicts of Interest: The authors declare no conflict of interest.

References

1. Best Research-Cell Efficiency Chart. Available online: https://www.nrel.gov/pv/cell-efficiency.html (accessed on 13 March 2022).
2. Taguchi, M.; Yano, A.; Tohoda, S.; Matsuyama, K.; Nakamura, Y.; Nishiwaki, T.; Fujita, K.; Maruyama, E. 24.7% Record Efficiency HIT Solar Cell on Thin Silicon Wafer. *IEEE J. Photovolt.* **2014**, *4*, 96–99. [CrossRef]
3. Würfel, U.; Cuevas, A.; Würfel, P. Charge Carrier Separation in Solar Cells. *IEEE J. Photovolt.* **2015**, *5*, 461–469. [CrossRef]
4. DeWolf, S.; Descoeudres, A.; Holman, Z.C.; Ballif, C. High-efficiency silicon heterojunction solar cells: A review. *Green* **2012**, *2*, 7–24. [CrossRef]
5. Feifel, M.; Ohlmann, J.; Benick, J.; Rachow, T.; Janz, S.; Hermle, M.; Dimroth, F.; Belz, J.; Beyer, A.; Volz, K.; et al. MOVPE Grown Gallium Phosphide–Silicon Heterojunction Solar Cells. *IEEE J. Photovolt.* **2017**, *7*, 502–507. [CrossRef]
6. Tsai, M.-L.; Su, S.-H.; Chang, J.-K.; Tsai, D.-S.; Chen, C.-H.; Wu, C.-I.; Li, L.-J.; Chen, L.-J.; He, J.-H. Monolayer MoS_2 Heterojunction Solar Cells. *ACS Nano* **2014**, *8*, 8317–8322. [CrossRef]
7. Sebenik, R.F.; Burkin, A.R.; Dorfler, R.R.; Laferty, J.M.; Leichtfried, G.; Meyer-Grünow, H.; Mitchell, P.C.H.; Vukasovich, M.S.; Church, D.A.; Van Riper, G.G.; et al. Molybdenum and Molybdenum Compounds. In *Ullmann's Encyclopedia of Industrial Chemistry*; John Wiley & Sons, Ltd.: New York, NY, USA, 2000; ISBN 978-3-527-30673-2.
8. Neville, R.A.; Evans, B.L. The Band Edge Excitons in 2H-MoS_2. *Phys. Status Solidi B* **1976**, *73*, 597–606. [CrossRef]
9. Mak, K.F.; Lee, C.; Hone, J.; Shan, J.; Heinz, T.F. Atomically Thin MoS 2: A New Direct-Gap Semiconductor. *Phys. Rev. Lett.* **2010**, *105*, 136805. [CrossRef]
10. Eda, G.; Yamaguchi, H.; Voiry, D.; Fujita, T.; Chen, M.; Chhowalla, M. Photoluminescence from Chemically Exfoliated MoS_2. *Nano Lett.* **2011**, *11*, 5111–5116. [CrossRef]
11. Song, I.; Park, C.; Choi, H.C. Synthesis and properties of molybdenum disulphide: From bulk to atomic layers. *RSC Adv.* **2015**, *5*, 7495–7514. [CrossRef]
12. Neto, A.H.C.; Novoselov, K. Two-Dimensional Crystals: Beyond Graphene. *Mater. Express* **2011**, *1*, 8. [CrossRef]
13. Novoselov, K.S.; Jiang, D.; Schedin, F.; Booth, T.J.; Khotkevich, V.V.; Morozov, S.V.; Geim, A.K. Two-dimensional atomic crystals. *Proc. Natl. Acad. Sci. USA* **2005**, *102*, 10451–10453. [CrossRef] [PubMed]

14. Xu, H.; Xin, L.; Liu, L.; Pang, D.; Jiao, Y.; Cong, R.; Yu, W. Large area MoS$_2$/Si heterojunction-based solar cell through sol-gel method. *Mater. Lett.* **2019**, *238*, 13–16. [CrossRef]

15. Huang, Y.; Shi, X.; Liu, X.; Cong, R.; Sun, Y.; Lu, W.; Yu, W. Boosting the photovoltaic performance of MoS$_2$/Si heterojunction solar cells with thiourea-doped MoS$_2$ films. *Micro Nanostruct.* **2022**, *167*, 207241. [CrossRef]

16. Cui, X.; Lee, G.-H.; Kim, Y.; Arefe, G.; Huang, P.; Lee, C.-H.; Chenet, D.; Zhang, X.; Wang, L.; Ye, F.; et al. Multi-terminal transport measurements of MoS2 using a van der Waals heterostructure device platform. *Nat. Nanotechnol.* **2015**, *10*, 534–540. [CrossRef]

17. Gao, J.; Li, B.; Tan, J.; Chow, P.; Lu, T.-M.; Koratkar, N. Aging of Transition Metal Dichalcogenide Monolayers. Available online: https://pubs.acs.org/doi/pdf/10.1021/acsnano.5b07677 (accessed on 9 February 2022).

18. Afanasiev, P.; Lorentz, C. Oxidation of Nanodispersed MoS$_2$ in Ambient Air: The Products and the Mechanistic Steps. *J. Phys. Chem. C* **2019**, *123*, 7486–7494. [CrossRef]

19. Martincová, J.; Otyepka, M.; Lazar, P. Is Single Layer MoS$_2$ Stable in the Air? *Chem. Eur. J.* **2017**, *23*, 13233–13239. [CrossRef]

20. Chhowalla, M.; Amaratunga, G.A.J. Thin films of fullerene-like MoS$_2$ nanoparticles with ultra-low friction and wear. *Nature* **2000**, *407*, 164–167. [CrossRef]

21. Du, G.; Guo, Z.; Wang, S.; Zeng, R.; Chen, Z.; Liu, H. Superior stability and high capacity of restacked molybdenum disulfide as anode material for lithium ion batteries. *Chem. Commun.* **2010**, *46*, 1106–1108. [CrossRef]

22. Park, S.; Mutz, N.; Schultz, T.; Blumstengel, S.; Han, A.; Aljarb, A.; Li, L.-J.; List-Kratochvil, E.J.W.; Amsalem, P.; Koch, N. Direct determination of monolayer MoS2and WSe2exciton binding energies on insulating and metallic substrates. *2D Mater.* **2018**, *5*, 025003. [CrossRef]

23. Ermolaev, G.A.; Stebunov, Y.V.; Vyshnevyy, A.A.; Tatarkin, D.E.; Yakubovsky, D.I.; Novikov, S.M.; Baranov, D.G.; Shegai, T.; Nikitin, A.Y.; Arsenin, A.V.; et al. Broadband optical properties of monolayer and bulk MoS$_2$. *Npj 2D Mater. Appl.* **2020**, *4*, 21. [CrossRef]

24. Bjelopavlić, D.; Pantić, D.; Đorđević, B.; Pantić, D. Simulation of hetero-junction silicon solar cells. *Contemp. Mater.* **2010**, *1*, 186–194. [CrossRef]

25. Ermachikhin, A.V.; Vorobyov, Y.V.; Maslov, A.D.; Trusov, E.P.; Litvinov, V.G. External Quantum Efficiency of Bifacial HIT Solar Cells. *Semiconductors* **2020**, *54*, 1254–1259. [CrossRef]

26. Dhyani, V.; Das, S. High-Speed Scalable Silicon-MoS$_2$ P-N Heterojunction Photodetectors. *Sci. Rep.* **2017**, *7*, 44243. [CrossRef] [PubMed]

27. Mukherjee, S. Novel Colloidal MoS$_2$ Quantum Dot Heterojunctions on Silicon Platforms for Multifunctional Optoelectronic Devices. *Sci. Rep.* **2016**, *6*, 29016. [CrossRef] [PubMed]

28. Davelou, D.; Kopidakis, G.; Kioseoglou, G.; Remediakis, I. MoS$_2$ nanostructures: Semiconductors with metallic edges. *Solid State Commun.* **2014**, *192*, 42–46. [CrossRef]

29. Zhang, Y.; Ye, J.; Matsuhashi, Y.; Iwasa, Y. Ambipolar MoS2 Thin Flake Transistors. Available online: https://pubs.acs.org/doi/pdf/10.1021/nl2021575 (accessed on 17 February 2022).